

Multitarget Vital Signs Measurement With Chest Motion Imaging Based on MIMO Radar

Chen Feng^{ID}, Xiaonan Jiang^{ID}, *Graduate Student Member, IEEE*, Min-Gyo Jeong, *Student Member, IEEE*, Hong Hong^{ID}, *Senior Member, IEEE*, Chang-Hong Fu^{ID}, *Member, IEEE*, Xiaohui Yang, E. Wang, Xiaohua Zhu^{ID}, *Member, IEEE*, and Xiaoguang Liu^{ID}, *Senior Member, IEEE*

Abstract—Simultaneous multitarget vital signs measurement has become a hot issue for noncontact vital signs perception. However, there is still challenge in the multitarget heartbeat measurement due to the weakness of heartbeat signal and interference from complex environment. In this article, a new multiple-input–multiple-output (MIMO) continuous-wave (CW) radar system equipped with 2-D digital beamforming (DBF) is presented to measure the respiration and heartbeat of multiple human subjects at unknown positions simultaneously. Through 2-D beam scanning of the whole scene, a 2-D radar image is generated. From the image, the chest motion of multiple targets is accurately located. Then, the vital signs of targets are obtained through forming individual beams focusing on the chests of targets. Moreover, the low intermediate frequency (low-IF) architecture is adopted to minimize the impact of flicker noise in low-frequency amplifier stages. The experimental results demonstrate that the proposed MIMO 2-D imaging radar system can locate chest areas of multiple targets, suppress the clutters, and make vital signs measurement, heartbeat measurement in particular, more robust compared with single-input–multiple-output (SIMO) radar system in complex environment.

Index Terms—Continuous wave (CW), multiple targets, multiple-input–multiple-output (MIMO), 2-D digital beamforming (DBF), vital signs.

I. INTRODUCTION

VITAL signs, such as respiration and heartbeat, are very important physiological indicators associated with many respiratory and cardiac diseases. Accurate and robust measurement of vital signs has been a very hot topic for many years.

Manuscript received December 24, 2020; revised February 28, 2021 and April 12, 2021; accepted April 17, 2021. Date of publication May 6, 2021; date of current version November 4, 2021. This work was supported in part by the National Key Research and Development Program of China under Grant 2020YFC2005302, in part by the National Natural Science Foundation of China under Grant 61871224, in part by the Key Research and Development Plan of Jiangsu Province under Grant BE2018729, in part by the Fundamental Research Funds for the Central Universities under Grant 30917011316, and in part by the Nanjing Integrated Traditional Chinese and Western Medicine Hospital (Ethical Approval Number 201812001). (*Chen Feng and Xiaonan Jiang are co-first authors.*) (*Corresponding author: Xiaohua Zhu.*)

Chen Feng, Hong Hong, Chang-Hong Fu, and Xiaohua Zhu are with the School of Electronic and Optical Engineering, Nanjing University of Science and Technology, Nanjing 210094, China (e-mail: hongnju@njust.edu.cn).

Xiaonan Jiang, Min-Gyo Jeong, and Xiaoguang Liu are with the School of Electrical and Computer Engineering, University of California, Davis, Davis, CA 95616 USA (e-mail: lxgliu@ucdavis.edu).

Xiaohui Yang is with the Nanjing Integrated Traditional Chinese and Western Medicine Hospital, Nanjing 210014, China (e-mail: 79260447@qq.com).

E. Wang is with the Department of Anesthesiology, Xiangya Hospital Central South University, Hunan 410008, China (e-mail: ewang324@csu.edu.cn).

Color versions of one or more figures in this article are available at <https://doi.org/10.1109/TMTT.2021.3076239>.

Digital Object Identifier 10.1109/TMTT.2021.3076239

Compared with traditional contact measurement methods such as respiration belt and electrocardiography [1], noncontact measurement methods have the advantage of no skin irritation and discomfort. Therefore, it is more suitable for infants monitoring, burn victims monitoring, and other long-term vital signs monitoring, such as sleep monitoring and sleep apnea detection [2]. Among noncontact approaches such as camera-, Wi-Fi-, and infrared-based, the microwave-based radar system is a promising candidate due to its high precision and accuracy, protection of personal privacy, and less dependence on lighting conditions.

In the past few decades, many research works have been devoted to the research of noncontact vital signs measurement based on radar principles. Several different radar types have been investigated in the field of noncontact vital signs measurement, such as continuous wave (CW) [3]–[5], pulse [6], and frequency-modulated CW (FMCW) [7]. At the same time, many novel processing methods of radar signal have been proposed, such as FTPR-based techniques and small-angle approximation [8]–[10]. However, most research focused on the vital signs measurement of a single target. To better cope with complex application scenarios, multitarget vital signs measurement has become an important research direction. Since motion induced by heartbeat is very weak and may be easily overwhelmed by clutters, there is still a challenge in the multitarget heartbeat measurement.

Currently, there are two main solutions to achieve the multitarget differentiation and vital signs measurement. One way is using range bins to separate different targets appeared in different range gates of the radar. Several different radar platforms have been explored for this solution, including FMCW [11]–[17], stepped frequency CW (SFCW) [18]–[29], and ultrawideband (UWB) [20]–[22]. Among them, Mercuri *et al.* [11] have utilized an FMCW radar to achieve spatial tracking and vital signs measurement of multiple targets during the desk work. Su *et al.* [18] have realized the simultaneous vital signs measurement of three targets located at different distances based on an SFCW radar. Although many studies have achieved very good results based on this category of methods, the limitation is that the vital signs of multiple targets could not be separated well when they are in the same range bin.

The other way is using spatially distributed beams to separate different targets from different angles. In more detail, there are three main approaches to achieve spatially distributed

beams, including metamaterial leaky-wave antenna (LWA), phased-array antenna (PAA), and digital beamforming (DBF). For the LWA-based solution, the beam scanning is achieved by changing the transmitting frequency at the cost of low spectrum efficiency [23]–[26]. For the PAA-based solution, the beamforming is achieved by using phase shifters to control the phase of each antenna element in a phased array [27], [28]. Nosrati *et al.* [27] built a phased-array multiple-input–multiple-output (MIMO) radar prototype to realize the measurement of respiratory rates of two targets at different azimuth angles by forming a concurrent dual beam to illuminate the two targets separately. However, the phase shifters used in this method dramatically increase the hardware complexity and cost. DBF technology is becoming more and more popular due to its advantages of simple hardware structure, control flexibility, and high accuracy [29]–[36]. Xiong *et al.* [29] realized simultaneous multitarget respiratory rate measurement by using the DBF technology based on a single-input–multiple-output (SIMO) radar. Sasakawa *et al.* [30]–[32] used an MIMO radar system with separate transmission and reception to achieve indoor multitarget positioning and vital signs measurement. Ahmad *et al.* [33] exploited the DBF ability of a TI FMCW MIMO radar to achieve vital signs measurement of two targets. However, the two subjects need to breathe alternately during the test. Other works to achieve multitarget vital signs measurement based on MIMO radar have also been published [43]–[45]. Despite these preliminary studies, robust multitarget vital signs measurement, especially multitarget heartbeat measurement, is still a big challenge because the echo signal related to heartbeat is relatively weak and can easily be overwhelmed by clutters.

As is well known, the principle of radar-based vital signs measurement is that the respiration and heartbeat drive the chest surface a tiny motion and then modulate the radar reflection signal. Therefore, locating the chest surface motion is beneficial to suppressing clutters and improving the robustness of vital signs measurement, especially the heartbeat measurement. Sakamoto *et al.* [34] achieved respiratory motion imaging based on an SIMO radar platform. However, this work focuses on the scene where a single target is lying down and does not involve heartbeat measurement.

In this article, an MIMO CW radar prototype is presented. The radar system consists of six transmitting channels and six receiving channels for 2-D DBF imaging. From the 2-D radar image, the chest motion of multiple targets is accurately located. Then, the vital signs of targets are obtained through forming individual beams focusing on the chests of targets. The proposed solution can effectively suppress clutters from nearby objects and small movements of other parts of the body, e.g., legs, head, and arms. As a result, the signal quality is significantly improved. To improve signal-to-noise ratio (SNR) for the very low-frequency vital signs signals, a low intermediate frequency (low-IF) architecture is used to minimize the impact of flicker noise in the baseband amplifier stages [38]. Several experiments are performed to demonstrate the superior vital signs measurement performance of the proposed MIMO radar prototype.

In short, the main contributions of this work are as follows.

- 1) The chest areas of multiple targets are accurately located with chest motion imaging. The vital signs measurement, especially the heartbeat measurement, is significantly enhanced by forming individual narrow beams focusing on the chest regions.
- 2) The proposed MIMO radar system is able to simultaneously measure the vital signs of closely spaced targets at the same distance from the radar. It provides a good solution for noncontact vital signs measurement of multiple targets in sleep monitoring scenarios.
- 3) It is the first time that the IF-CW mode is applied to an MIMO radar system. It can minimize the impact of flicker noise in the baseband amplifier stages and significantly improve the quality of the received signal.

The rest of this article is organized as follows. Section II introduces the fundamental theory of DBF and virtual array based on MIMO radar. In Section III, the MIMO radar system design is illustrated. Section IV presents the experimental setup and results. Section V contains further discussions, and Section VI provides the conclusion.

II. FUNDAMENTAL THEORY

A. Basic of DBF

The electronically controlled beam-scanning capability is one of the most important characteristics of phased-array antennas. The received or transmitted signals of two adjacent antenna elements of the array have a fixed phase difference depending on the steering angle. Beamforming can be achieved by combining signals from multiple transmit and receive antenna pairs.

The 2-D DBF theory based on planar array is an extended version of the 1-D DBF theory based on linear array. For the sake of simplicity, the 1-D DBF theory of uniform linear array (ULA) is introduced in this section.

Fig. 1(a) shows a typical receiving architecture of a ULA with M channels. The incident signal of a far-field target with the incident angle θ_r to the k th receiving antenna can be expressed as

$$\begin{aligned} u_k(t) &= T(t - \tau_k) \\ &= e^{j[2\pi f_0(t-\tau_k)+\varphi_{(t-\tau_k)}]} \\ &= e^{j[2\pi f_0 t + \varphi_{(t-\tau_k)}]} \cdot e^{-j2\pi f_0 \tau_k}, \quad k \in [1, M] \end{aligned} \quad (1)$$

where $T(t) = e^{j(2\pi f_0 t + \varphi_t)}$ denotes the transmitted signal, f_0 is the carrier frequency, and τ_k is the time delay to the k th receiving channel. Assuming that τ_k is short enough that the change of the φ_t can be ignored, then (1) can be simplified as

$$u_k(t) \approx T(t)e^{-j2\pi f_0 \tau_k}. \quad (2)$$

The incident signal to the $(k+1)$ th receiving antenna can be expressed as

$$\begin{aligned} u_{k+1}(t) &\approx T(t)e^{-j2\pi f_0 \tau_{k+1}} \\ &= T(t)e^{-j2\pi f_0 (\tau_k + \Delta \tau)} \\ &= u_k(t)e^{-j2\pi f_0 \Delta \tau} \end{aligned} \quad (3)$$

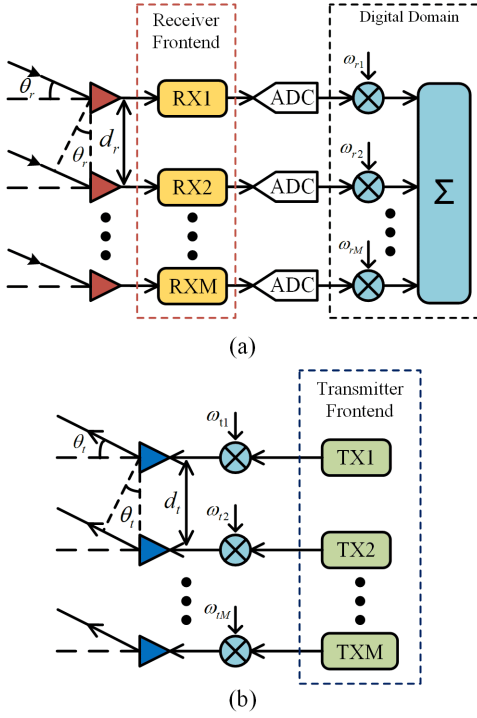


Fig. 1. (a) Receiving architecture of ULA. (b) Transmitting architecture of ULA.

where $\Delta\tau$ is the time delay difference between two adjacent receiving channels. It depends on the wave path difference between the two channels

$$\begin{aligned}\Delta\tau &= \frac{\Delta r}{c} \\ &= \frac{d_r \sin \theta_r}{c}\end{aligned}\quad (4)$$

where Δr and d_r are the wave path difference and the distance between two adjacent receiving channels, respectively.

Taking the first channel as the reference, the receiving signal of the K th channel can be written as

$$\begin{aligned}u_k &= u_1 e^{-j2\pi f_0(k-1)\Delta\tau} \\ &= u_1 e^{-j2\pi f_0(k-1) \frac{d_r \sin \theta_r}{c}} \\ &= u_1 e^{-j(k-1)2\pi \frac{d_r \sin \theta_r}{\lambda}}\end{aligned}\quad (5)$$

where λ is the wavelength of the transmitted signal.

Finally, according to (5), the steering vector $v(\theta_r)$ of the receiving array at the angle of θ_r is achieved

$$v(\theta_r) = [1, e^{-j2\pi \frac{d_r \sin \theta_r}{\lambda}}, \dots, e^{-j(M-1)2\pi \frac{d_r \sin \theta_r}{\lambda}}]. \quad (6)$$

The steering vector $v(\theta_t)$ of the transmitting array at the angle of θ_t can be derived in the same way

$$v(\theta_t) = [1, e^{-j2\pi \frac{d_t \sin \theta_t}{\lambda}}, \dots, e^{-j(M-1)2\pi \frac{d_t \sin \theta_t}{\lambda}}]. \quad (7)$$

The simulation result of DBF based on a six-element ULA with half-wavelength distance between two adjacent antennas is shown in Fig. 2. The 3-dB beamwidth of a ULA is proportional to the steering angle and inversely proportional

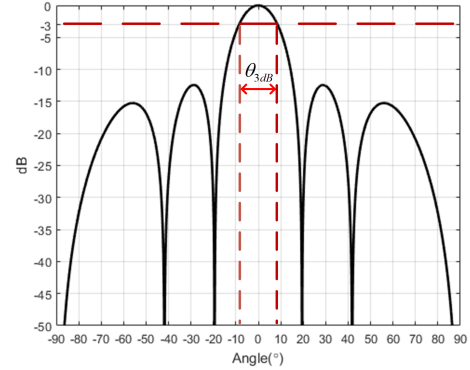


Fig. 2. DBF simulation of a six-element ULA.

to the number of array elements [42]

$$\theta_{3dB} \approx \frac{1}{\cos \theta_s} \frac{50.8\lambda}{Nd} (\circ) \quad (8)$$

where θ_s denotes the steering angle, N denotes the element number of the ULA, d denotes the distance between two adjacent antennas, and λ denotes the transmitting wavelength.

B. MIMO Radar

In order to achieve 2-D beam scanning, one conventional way is to transmit a single beam to a specific angle with simultaneously forming the receiving beam at the same angle and then scanning the desired region by stepping the angle. Obviously, this method is very time-consuming [37]. Another way is to use a planar phased array to form a 2-D beam directly. Although this approach can achieve fast scanning of the desired region, the hardware complexity and system cost are usually significant.

Since the radiation pattern of an array in the far field is the Fourier transform of the array distribution, the equivalent radiation pattern of an MIMO radar can be calculated as the Fourier transform of the convolution of the transmitter array and the receiver array. This convolution is referred to as the virtual array [37], [40]. Therefore, an MIMO radar system could be viewed as a virtual planar phased array. It can realize fast 2-D beam scanning with low hardware cost.

An MIMO radar consisting of an M -element transmitting ULA and an N -element receiving ULA is considered in this article. The inverted L-shaped geometry of the MIMO radar and its corresponding virtual array are shown in Fig. 3, where the horizontally distributed red elements are the receivers, the vertically distributed blue elements are the transmitters, and the black ones are the corresponding virtual elements. As shown in Fig. 3, the MIMO radar is equivalent to an $M \times N$ element virtual planar array. For convenience, each virtual element is noted as (p, q) , where p and q denote the row and the column of the array, respectively. Based on the $M \times N$ -element virtual planar array, a 2-D beam with a specific zenith angle θ_t and azimuth angle θ_r can be achieved by the DBF theory

$$R(\theta_t, \theta_r) = v^T(\theta_t) \times S \times v(\theta_r) \quad (9)$$

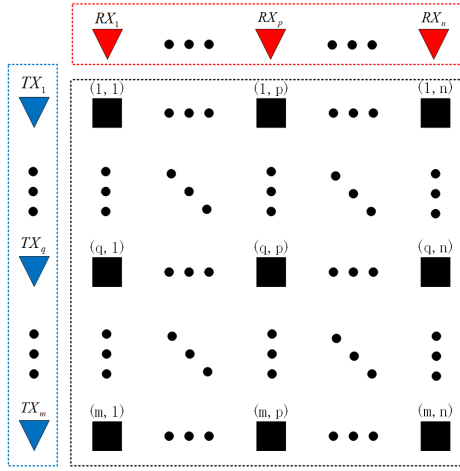


Fig. 3. Geometries of the MIMO radar and its corresponding virtual array.

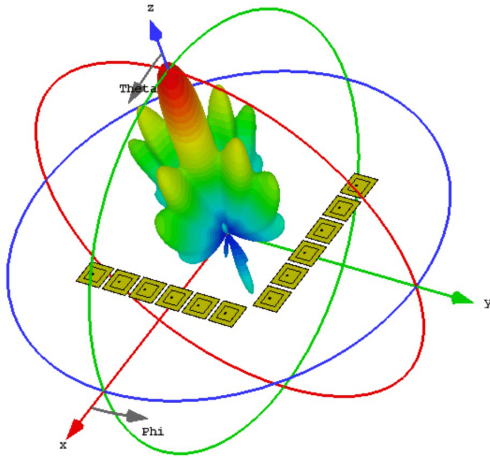


Fig. 4. 2-D beam pattern based on MIMO radar.

where

$$S = \begin{bmatrix} s_{(1,1)} & s_{(1,2)} & \cdots & s_{(1,n)} \\ s_{(2,1)} & s_{(2,2)} & \cdots & s_{(2,n)} \\ \vdots & \vdots & \ddots & \vdots \\ s_{(m,1)} & s_{(m,2)} & \cdots & s_{(m,n)} \end{bmatrix} \quad (10)$$

$v^T(\theta_t)$ is the transpose of the transmitting steering vector and $v(\theta_r)$ is the receiving steering vector which both can refer to Section II-A. $s_{(p,q)}$ ($p \in [1, n]$, $q \in [1, m]$) is the quadrature demodulated signal of the echo transmitted by the p th transmitter and received by the q th receiver.

A 2-D beam pattern steered to the center of the array (zenith angle $\theta_t = 0^\circ$ and azimuth angle $\theta_r = 0^\circ$) based on a 6×6 MIMO radar is shown in Fig. 4. The 2-D beam scanning of the area is achieved by changing θ_t and θ_r with the step angle of 1° . An image is obtained after the scanning of the scene.

III. SYSTEM DESIGN

A proof-of-concept dual-PLL-based low-IF MIMO radar is designed and implemented in this article. The MIMO radar

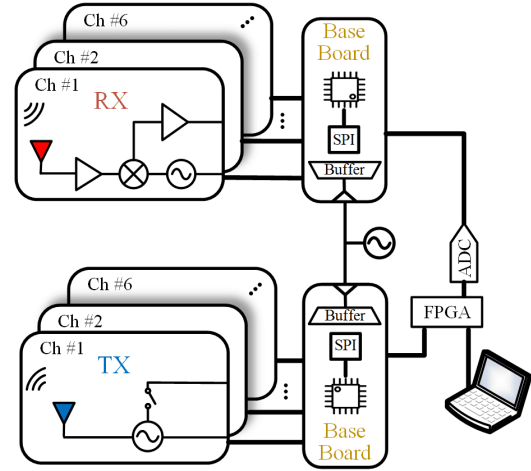


Fig. 5. Block diagram of the MIMO radar.

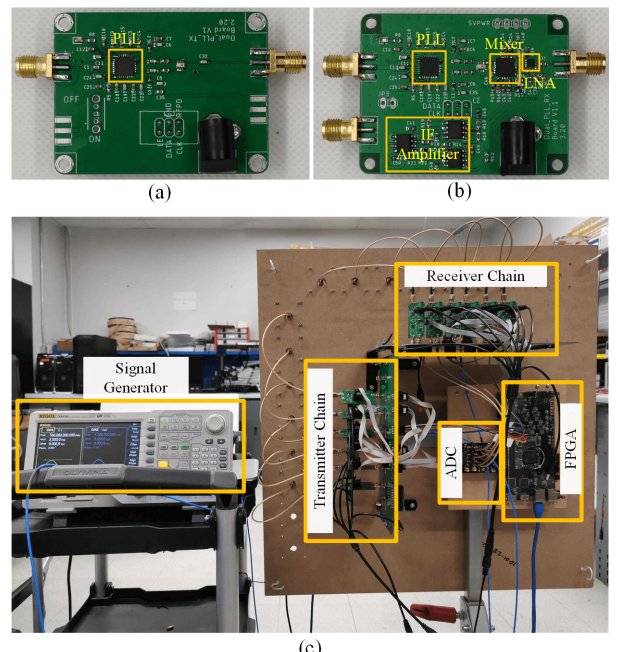


Fig. 6. Photograph of the MIMO radar. (a) Single transmitter. (b) Single receiver. (c) Overview of the system.

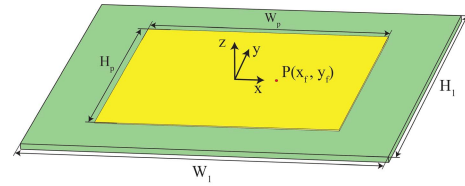


Fig. 7. Geometry of the probe-fed microstrip patch antenna.

consists of six transmitting and six receiving channels. The system operates at 2.45 GHz in the CW mode. Fig. 5 shows the block diagram of the proposed MIMO radar and Fig. 6 shows a photograph of the actual assembled system. The system consists of an antenna array, RF transceivers, and the baseband

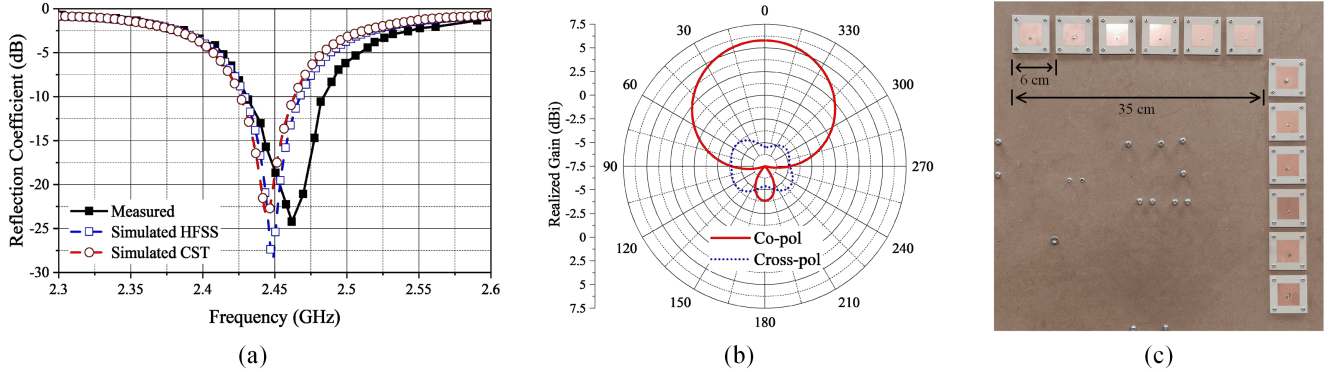


Fig. 8. (a) Simulated and measured reflection coefficients of the designed antenna. (b) Simulated radiation pattern of the designed antenna. (c) Photograph of the antenna array.

TABLE I
KEY COMPONENTS USED IN THE SYSTEM

Component	Manufacture	Role
ADF4351	Analog Device	PLL
ADL5265	Analog Device	Passive Mixer
QPL9057	Qorvo	LNA
OP07	Analog Device	IF amplifier
CDCLVC1108	Texas Instrument	1:8 Clock Buffer
L4941	STMicroelectronics	5V LDO
ADP150	Analog Device	3.3V LDO
Teensy 3.2	PJRC	Microcontroller
Artix-7 XC7A100T	XILINX	FPGA
AD7606	Analog Device	ADC

TABLE II
DIMENSIONS OF THE DESIGNED PATCH ANTENNA

W_1	H_1	W_p	H_p	x_f	y_f
53.25	52.5	31	31	5	0

Unit: mm

signal processing module. All modules except the signal generator are fixed on a board, the antenna array is on the front of the fixture, and the remaining modules are on the back. The key components used in the system are listed in Table I.

A. Antenna Array Design

In this article, a standard probe-fed microstrip patch antenna is used (see Fig. 7). The antenna is designed for Rogers Ro4003C substrate with a thickness of 0.508 mm. The design parameters, including the width and height of the substrate and the ground plane (W_1 and H_1), the width and height of the patch (W_p and H_p), and the probe-feeding position along the x - and y -axes (x_f and y_f), are given in Table II.

The single antenna is simulated on CST Microwave Studio 2020 (CST) and Ansys Electronics Desktop 2020 R2 (HFSS) and measured using an Agilent Technologies E5071A Network Analyzer in an anechoic chamber. Fig. 8(a) shows a

comparison of two simulated and one measured reflection coefficients of the antenna. Although there is a slight frequency shift in the measured result, the measured impedance bandwidth covers 2.43–2.476 GHz. Besides, the simulated radiation pattern of the antenna is given in Fig. 8(b). The maximum realized gain is approximately 5.6 dBi and the front-to-back ratio is approximately 10 dB. The MIMO array of the radar is formed by six transmitting and six receiving antennas in an inverted L shape, as shown in Fig. 8(c). The distance between two adjacent antennas is 6 cm.

B. Transceiver Design

The MIMO radar transceiver consists of six transmitter modules and six receiver modules. All modules share the same reference signal. The low-IF architecture is adopted by generating a 1-kHz frequency difference between the transmitted signal and the LO signal [38]. The electronic circuits, including the transmitters, receivers, and baseboards, are fabricated using four-layer PCBs.

1) *Transmitter Design:* Fig. 6(a) shows the front side of the fabricated transmitter module. It contains a PLL IC as well as its peripheral circuits. In this setup, the TX module takes a 100-MHz clock from the baseboard and output a 2.45 GHz + 1 kHz RF signal with a power level of 0 dBm. Six identical transmitters connected to a baseboard form the transmitter chain of the MIMO radar. The backside of the transmitter module contains power management circuits for the generation of the different voltages required by the circuits. The back of the receiver module shares the same design.

In order to distinguish different TX signals while they share the same frequency, time-division multiplexing (TDM) is adopted to ensure that only one transmitter works at a time. The switching of the RF source is realized by applying a digital enable signal generated by an FPGA.

2) *Receiver Design:* Fig. 6(b) shows the front side of the fabricated receiver. The core components include a PLL IC, a mixer IC, a low-noise amplifier (LNA), and a two-stage IF amplifier. In this setup, the PLL takes a 100-MHz clock signal from the baseboard and outputs a 2.45-GHz RF signal with a power level of 0 dBm. The signal is then fed to the LO port of the mixer. On the other hand, the receiving signal is

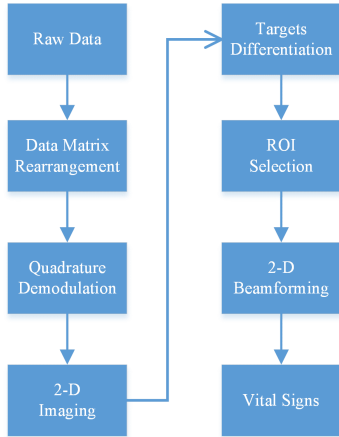


Fig. 9. Flow of the baseband signal processing algorithm.

acquired by the antenna and amplified by the LNA with a gain of 20 dB. Then, the amplified signal is fed to the RF port of the mixer. Due to the frequency difference between the received signal and the LO signal, a 1-kHz low-IF baseband signal is generated by the mixer. The baseband signal goes through a two-stage differential-to-single-ended IF amplifier with a gain of 30 dB. Six identical receivers connected to a baseboard form the receiver chain of the MIMO radar. Unlike the TX modules working in TDM mode, the RX modules operate all at the same time.

3) *Baseboard Design:* The key for the multi-PLL system working correctly is to provide the same reference clock to each PLL IC. Therefore, a clock distribution baseboard is utilized to split the input clock into multiple outputs. It also serves to provide the configuration signals and structural support for the transmitter boards and receiver boards. The core components of the clock distribution board include a one-to-eight clock buffer, a microcontroller, and voltage regulators. Two baseboards are used for the transmitter chain and the receiver chain, respectively. The 100-MHz clock output of the Rigol DG4162 signal generator is split into two paths connected to the clock buffers of the two baseboards. In each baseboard, the clock signal is further split into eight paths, which ensures that the PLLs of the transmitters and receivers are locked to the same reference. The microcontroller is used to configure the PLLs when the system is powered ON.

C. Baseband Signal Processing

1) *Sampling Design:* In order to sample the six-channel output signals of the receiver chain simultaneously, an eight-channel analog-to-digital converter (ADC, AD7606) is used at a sampling rate of 50 ks/s. As introduced in Section III-B, the six transmitters are turned on one after another. The working duration of each transmitter in each cycle is (1/150) second, which means that it takes (1/25) second for the MIMO radar to complete a full scan. Therefore, the equivalent sampling frequency is 25 Hz. During the wake-up process of each transmitter, a label indicating the current transmitter number is generated by the FPGA and inserted at the beginning of the corresponding sampling data. Then, the data stream composed

of sampling data and labels is transmitted from the FPGA to a host computer through an Ethernet cable.

2) *Signal Processing:* The baseband signal processing algorithm is designed and implemented in MATLAB. The processing flow of the algorithm is shown in Fig. 9. The first step after sampling is to rearrange the raw data. With the labels at the beginning of the data stream, the sampling data corresponding to different transmitters and receivers can be separated accurately and a data matrix is obtained. Then, quadrature demodulation is applied to the data matrix. An image is then generated through 2-D beam scanning of the whole scene in the digital domain. From the image, the region of interest (ROI), which represents the most significant motion of the chests, can be located for multiple targets. Finally, the vital signs of targets are obtained through forming individual beams focusing on these ROIs.

IV. EXPERIMENT

Four sets of experiments are performed to evaluate the performance of the proposed MIMO radar prototype. Experiment 1 is performed to verify the accuracy of the beam formed by the radar. Experiments 2 and 3 are performed to demonstrate the multitarget vital signs measurement performance of the radar. Finally, Experiment 4 is performed to explore the resolution performance of the radar system. In Experiments 2–4, a breathing belt (iWorx RM-200) and finger-clipped pulse oximeter sensor (TI AFE4490 EVM) are used to provide the ground truth of the subjects' respiratory rate and heart rate. Two male volunteers with ages of 28 and 25, weights of 63 and 81 kg, and heights of 1.72 and 1.78 m participate in the experiments. They both are healthy and do not have any respiratory or heart diseases. All experiments are done in a laboratory with various electronic instruments.

A. System Calibration

Calibration is a necessary setup for the proposed MIMO radar. The aim of calibration is to compensate for the different amplitude and phase responses of different channels. Since this imbalance between channels is only caused by the radar system, e.g., components variations and fabrication tolerances, it is independent of the operative scenario or the distance of the targets in theory. It is unnecessary to repeat the calibration procedure when the target distance changes. The setup of calibration is shown in Fig. 10(a). A linear motor with a small metal plate fixed on it is placed 2-m away in front of the radar. The size of the plate is 10 × 10 cm and its material is copper. The centers of the plate and the antenna array are aligned. The motor is programmed to move in a sine-wave trajectory with the amplitude of 1 cm at a frequency of 1.2 Hz. After 30 s of sampling, the echo signals of 36 channels corresponding to Tx1–Tx6 and Rx1–Rx6 are obtained. The corresponding demodulated signals are achieved

$$C_k(t) = a_k e^{j(\omega_d t + \varphi_k)} + b_k e^{j\phi_k}, \quad k \in [1, 36] \quad (11)$$

where $\omega_d = 2\pi \times 1.2$ Hz is the Doppler frequency of the target, $b_k e^{j\phi_k}$ is the noise, and a_k and φ_k denote the amplitude

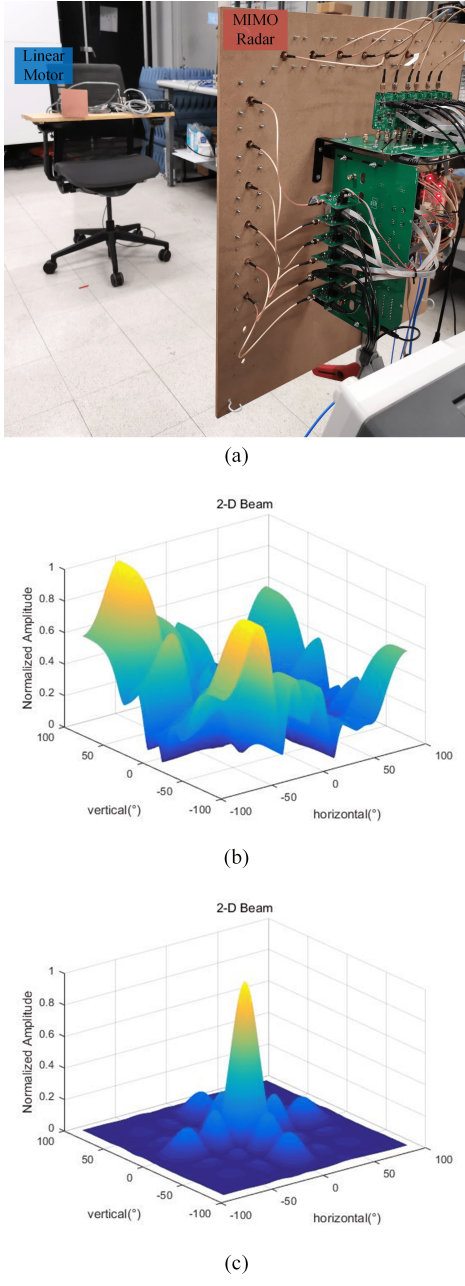


Fig. 10. System calibration. (a) Experimental setup of the calibration. (b) 2-D beam before calibration. (c) 2-D beam after calibration.

and the initial phase of the k th channel. Then, the Fourier transform is utilized to derive a_k and φ_k

$$C_k(\omega) = 2\pi(\sigma(\omega - \omega_d)a_k e^{j\varphi_k} + \sigma(\omega)b_n e^{j\phi_k}) \quad (12)$$

where $\sigma(\omega)$ is the impulse function. Finally, the calibration coefficients are obtained as

$$W = \left[\frac{e^{-j\varphi_1}}{a_1} \frac{e^{-j\varphi_2}}{a_2} \dots \frac{e^{-j\varphi_{36}}}{a_{36}} \right]. \quad (13)$$

The beam steered at $(0^\circ, 0^\circ)$ before the system calibration is shown in Fig. 10(b), and the beam after the system calibration is shown in Fig. 10(c). It is obvious that without calibration, the imbalance between various channels will result in the failure to form a correct and clean beam.

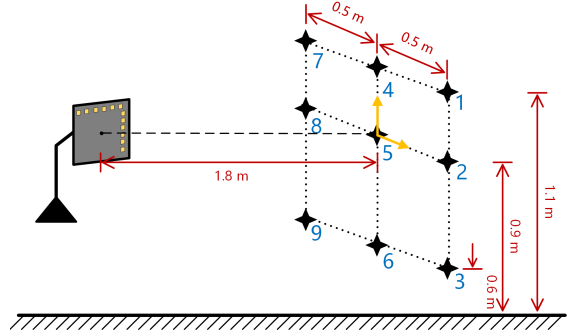


Fig. 11. Setup of Experiment 1. Nine black four-pointed stars in a plane which is parallel to the antenna array represent testing points. The distance between radar and testing plane is 1.8 m.

B. Accuracy Verification of the 2-D Beam

Experiment 1 is designed to verify the accuracy of the beam formed by the radar. The setup of the experiment is shown in Fig. 11. The radar prototype is installed on a tripod with the antenna array perpendicular to the ground. The center of the antenna array is 0.9 m from the ground. In a vertical plane that is 1.8 m away from the antenna array, nine points are selected as the testing points that are marked with black four-pointed stars in Fig. 11. Among them, Point 5 is located at the intersection of the central axis of the antenna array and the testing plane. Using Point 5 as the reference, the relative positions of other points can be calculated based on the measured distance. For example, the position of Point 1 is $(0.5 \text{ m}, 0.2 \text{ m})$, where 0.5 m denotes the horizontal position and 0.2 m denotes the vertical position. Then, the distance coordinates can be converted to angle coordinates relative to the center of the antenna array according to the trigonometric formula

$$\begin{aligned} \theta_h &= \arctan\left(\frac{x}{D}\right) \div \pi \times 180^\circ \\ \theta_v &= \arctan\left(\frac{y}{D}\right) \div \pi \times 180^\circ \end{aligned} \quad (14)$$

where θ_h and θ_v are the horizontal and vertical angles, respectively, x and y are the horizontal and vertical coordinates, respectively, and $D = 1.8 \text{ m}$ is the radial distance between the subject and the radar. For Point 1, the calculated angle coordinate is $(15.5^\circ, 6.3^\circ)$. A linear motor that is programmed to move in a sine-wave trajectory with the amplitude of 1 cm at a frequency of 1.2 Hz is placed at the nine testing points in sequence. The results are shown in Table III. Among nine testing points, the maximum error between the radar measured angles and the theoretical calculated angels is 1.5° in the horizontal direction and 1.3° in the vertical direction. Considering that the step angle of the beam scanning is 1° , the beam formed by radar is shown to be reasonably accurate.

C. Chest Motion Imaging and Vital Signs Measurement of Two Sitting Subjects

The setup of Experiment 2 is shown in Fig. 12. Similar to Experiment 1, the radar prototype is installed on a tripod. Two volunteers sit in front of the radar and face the antenna

TABLE III
ACCURACY VERIFICATION OF THE ANGLE OF THE BEAM

Point Number	Distance Coordinate ¹	Calculated Angle ²	Detected Angle ²
1	(0.5, 0.2)	(15.5, 6.3)	(16, 5)
2	(0.5, 0.0)	(15.5, 0.0)	(16, 0)
3	(0.5, -0.3)	(15.5, -9.5)	(16, -10)
4	(0.0, 0.2)	(0.0, 6.3)	(1, 6)
5	(0.0, 0.0)	(0.0, 0.0)	(0, 1)
6	(0.0, -0.3)	(0.0, -9.5)	(1, -10)
7	(-0.5, 0.2)	(-15.5, 6.3)	(-15, 5)
8	(-0.5, 0.0)	(-15.5, 0.0)	(-14, 0)
9	(-0.5, -0.3)	(-15.5, -9.5)	(-14, -9)

¹ Unit of Distance: m

² Unit of Angle: °

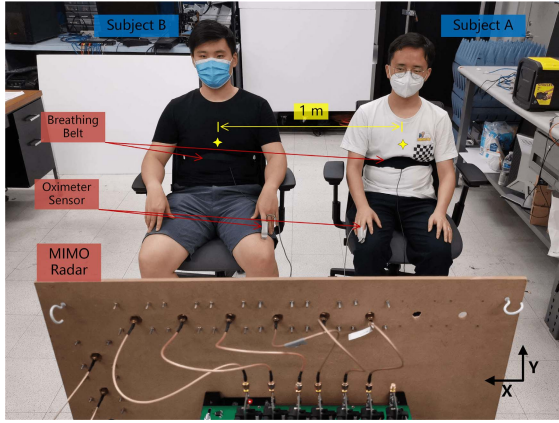


Fig. 12. Setup of Experiment-2: the multitarget vital signs measurement of sitting people.

array. The radial distance between the radar and volunteers is 1.8 m. Utilizing the coordinate system described in Fig. 11 and Section IV-B, the chest positions of Subjects A and B are represented by $A(0.5 \text{ m}, -0.15 \text{ m})$ and $B(-0.5 \text{ m}, -0.2 \text{ m})$. According to (14), the corresponding calculated angle coordinates are $A(15^\circ, -5^\circ)$ and $B(-15^\circ, -6^\circ)$. Two breathing belts and finger-clipped pulse oximeter sensors are used to record the ground-truth respiratory and heart rate of the two volunteers. The volunteers are instructed to remain calm and to breathe normally during the measurement.

In the experiment, the chest motion image of two subjects is formed after the 2-D beam scanning by radar. As shown in Fig. 13(a), the most significant motion is located at $A(17^\circ, -5^\circ)$ and $B(-13^\circ, -7^\circ)$ corresponding to the chest areas of the two subjects, respectively. This is consistent with the angle coordinates calculated above.

Then, the proposed vital signs measurement is performed by forming a concurrent 2-D dual beam steered at these two regions. The time-domain waveform of Subject A is shown in Fig. 13(b). A Fourier analysis is performed on the waveform and the frequency spectrum of 0–1 Hz is extracted and shown in Fig. 13(d). It is noted that the respiratory rate of adult is usually under 60 bpm. In the desired range, the frequency peak

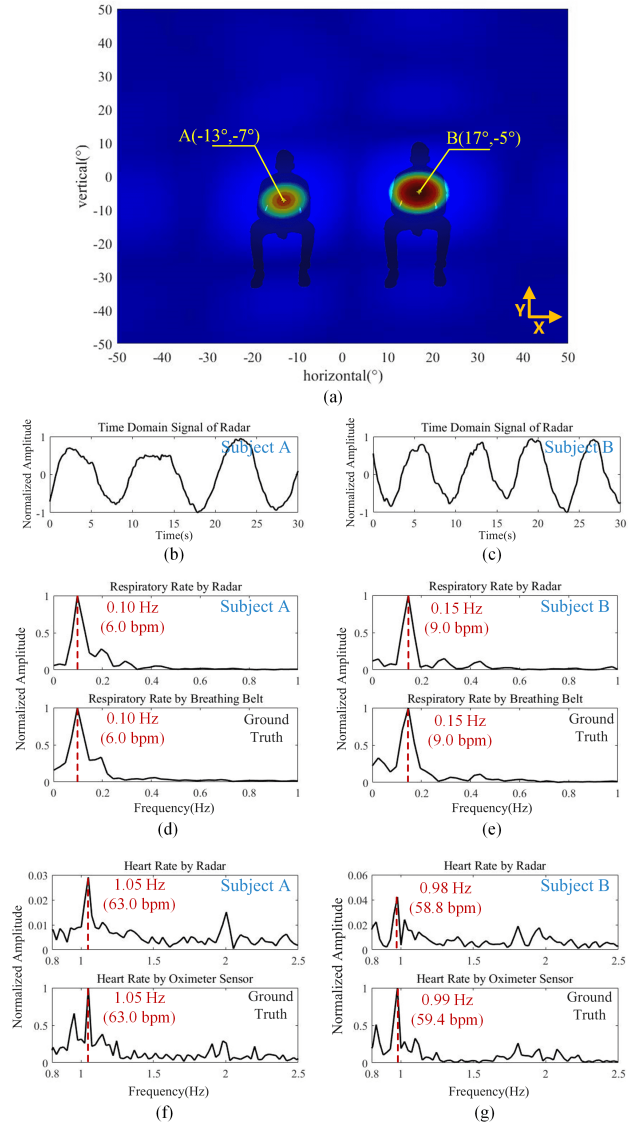


Fig. 13. Results of Experiment-2. (a) Result of chest motion imaging. (b) Time-domain waveform of Subject A. (c) Time-domain waveform of Subject B. (d) Frequency spectrum of respiratory rate of Subject A. (e) Frequency spectrum of respiratory rate of Subject B. (f) Frequency spectrum of heartbeat rate of Subject A. (g) Frequency spectrum of heartbeat rate of Subject B.

of 0.10 Hz is detected and the respiratory rate is calculated as 6.0 bpm. It is consistent with the ground truth measured by the breathing belt as shown in the figure. At the same time, the spectrum of 0.8–2.5 Hz is extracted in Fig. 13(f) for the measurement of the heart rate. It is demonstrated that the measured heart rate of 1.05 Hz (63.0 bpm) is also accurate compared with the ground truth from the oximeter sensor. The results of Subject B are shown in Fig. 13(c), (e), and (g), showing comparable accuracy to the case of Subject A.

Then, the experiment is repeated ten times and each measurement is 120 s long. A sliding window of 25 s with overlap of 20 s is used to process the data. It means that 200 estimations are performed for each subject and a total of 400 estimations are performed for two subjects. The detection success rate is defined as the percentage of the estimations



Fig. 14. Setup of Experiment 3: the multitarget vital signs measurement of lying people.

that the measured respiratory rate and heartbeat rate and their ground truth match within 1.5 and 3 bpm, respectively. The detection success rates of the respiratory rate measurement and heartbeat measurement for two subjects are 97.8% and 93.6%, respectively.

D. Chest Motion Imaging and Vital Signs Measurement of Two Lying Subjects

A potential application scenario of the proposed radar system is the sleep quality monitoring of multiple peoples. As shown in Fig. 14, the setup of Experiment 3 is to verify the performance of the proposed system in this scenario. The radar prototype is hung above a Styrofoam bed with the antenna array facing down toward the floor. Two volunteers lie on the bed facing the array in opposite orientations, and the distance between them is 0.8 m. The distance between the surface of the array and the bed is 1.9 m. The bed is 1.8 m wide and 2.4 m long. The same set of breathing belts and oximeter sensors as Experiment 2 is used to capture the ground truth. For the sake of convenience, the direction along the width of the bed is marked as the x -direction, and the length is in the y -direction.

As shown in Fig. 15(a), the most significant motion located by the imaging radar is at $A(-10^\circ, 9^\circ)$ and $B(15^\circ, -15^\circ)$, which is quite close to the actual chest position $A(-10^\circ, 10^\circ)$ and $B(15^\circ, -15^\circ)$. By forming a concurrent dual beam steered at these two ROIs, the echo signals are captured for further processing. After baseband signal processing, the vital signs of the two subjects are obtained and the results are shown in Fig. 15. The respiratory rate and heart rate measured by the radar are 0.15 Hz (9.0 bpm) and 1.1 Hz (66.0 bpm) for Subject A and 0.22 Hz (13.2 bpm) and 1.15 Hz (69.0 bpm) for

TABLE IV
RESOLUTION PERFORMANCE OF THE MIMO RADAR

Separation Distance ¹	Calculated Angle ²	Minimum Angle ³	Distinguish (Y/N) ⁴
0.8	24	17.1	Y
0.7	21	17.1	Y
0.6	18	17.2	Y
0.5	15	17.3	N

¹ Unit of Distance: m

² Unit of Angle: °

³ The minimum angle that the radar can not distinguish; Unit of Angle: °

⁴ Y/N: Yes/No

Subject B, respectively. As shown in the figures, the results of vital signs measurement match the ground truth very well in this experiment. Then, the experiment is repeated ten times and the detection success rate introduced in Section IV-C is utilized to evaluate the performance of the MIMO radar in this scenario. The detection success rates of the respiratory rate measurement and heartbeat measurement for two subjects are 98.4% and 92.6%, respectively.

E. Resolution Performance of the MIMO Radar

In the sleep scenario, the difficulty of separating the chest motion of multiple subjects increases as the distance between them decreases. Experiment 4 is performed to explore the resolution performance of the proposed MIMO radar. The setup of the experiment is almost the same as Experiment 3, as shown in Fig. 14. The only difference is that the two volunteers lie in the same orientation in this case. In this scenario, the coordinates of the two volunteers are approximately the same in the Y -direction. The experiment is performed with the distance between them reducing from 0.8 to 0.5 m in steps of 0.1 m, as shown in Fig. 16. Table IV shows the results of the experiment. At a distance of 0.5 m, the two volunteers almost lie shoulder by shoulder and their angular separation in the X -direction is approximately 15°. According to (8), the theoretical minimum beamwidth could be calculated as 17°. This closely matches the measurement results shown in Table IV.

V. DISCUSSION

A. MIMO Versus SIMO

Several articles [29], [35], [36] have realized multitarget vital signs measurement based on SIMO radar. In order to compare the performance of SIMO and MIMO radar in multitarget vital signs measurement, an experiment is performed with the same setup shown in Fig. 12. The proposed radar system is configured to work in SIMO mode by turning on only one transmitter. The results are shown in Fig. 17. As shown in Fig. 17(a), two targets at different horizontal angles can be separated using the 1-D beamforming capability of SIMO radar. However, the width of the beam in the vertical direction is very large. It is impossible to focus only on the chests of targets. As a result, the result is susceptible to

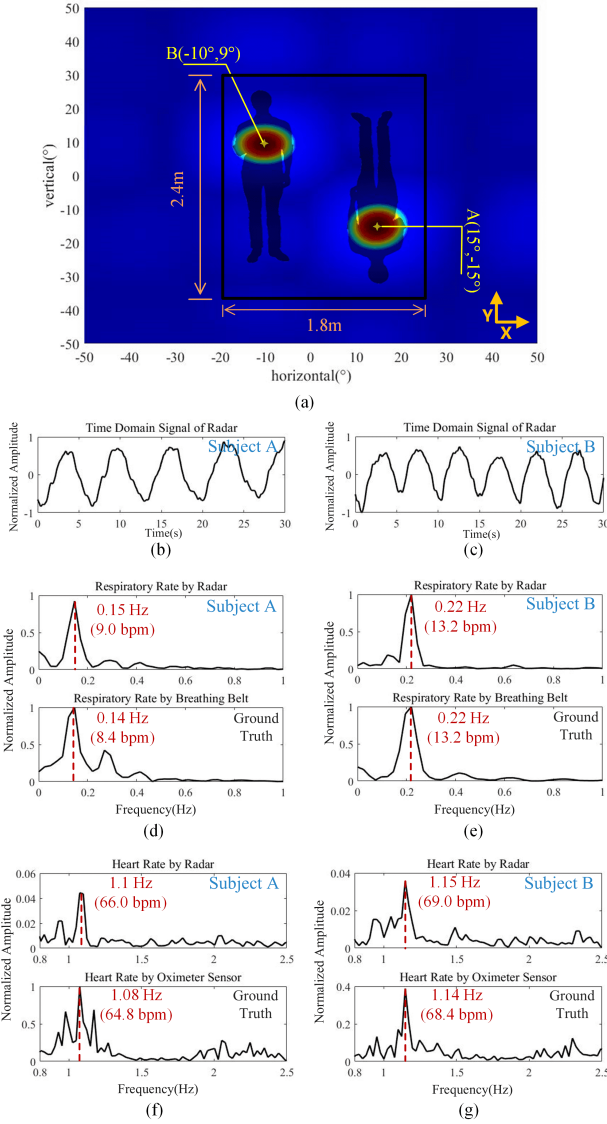


Fig. 15. Results of Experiment 3. (a) Result of chest motion imaging. (b) Time-domain waveform of Subject A. (c) Time-domain waveform of Subject B. (d) Frequency spectrum of respiratory rate of Subject A. (e) Frequency spectrum of respiratory rate of Subject B. (f) Frequency spectrum of heartbeat rate of Subject A. (g) Frequency spectrum of heartbeat rate of Subject B.

clutters from the complex environment and small movements of other parts of the body, e.g. legs and head. As shown in Fig. 17(c) and (e), although the respiratory rate of the targets can be detected by SIMO radar, the SNR of the heartbeat signal is very low. For Subject A, the heartbeat signal has been overwhelmed by clutters. In comparison, the experimental results of MIMO radar are shown in Fig. 17(b), (d), and (f). The respiratory rate and heartbeat rate of the targets can be easily detected by MIMO radar in the same experimental conditions.

B. Comparison With Other Relevant Works Based on MIMO Radar

Until now, several articles focusing on multitarget vital signs detection and human localization based on MIMO radar have

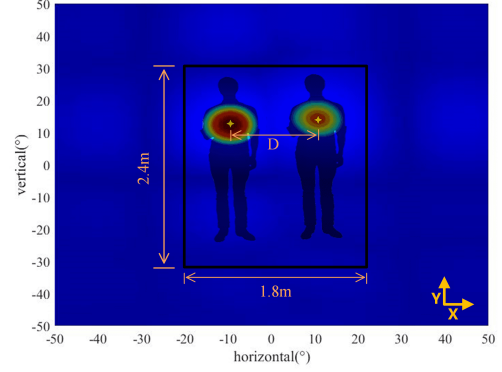


Fig. 16. Result of Experiment 4: chest motion imaging of two subjects lying in the same orientation and D represents the distance between them in the X -direction.

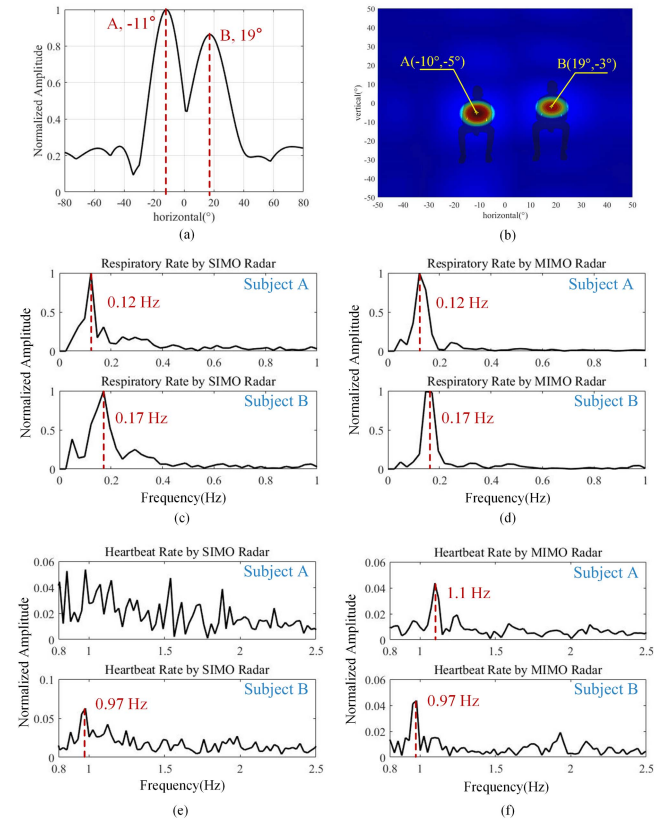


Fig. 17. Comparison of MIMO radar and SIMO radar. (a) Result of beamforming by SIMO radar. (b) Result of chest motion imaging by MIMO radar. (c) Frequency spectrum of respiratory rate of two subjects measured by SIMO radar. (d) Frequency spectrum of respiratory rate of two subjects measured by MIMO radar. (e) Frequency spectrum of heartbeat rate of two subjects measured by SIMO radar. (f) Frequency spectrum of heartbeat rate of two subjects measured by MIMO radar.

been published [46]. The main properties of these articles are summarized in Table V. In [30], fast living-body localization is achieved by applying the MUSIC method to the time-differential channel. In [27], [29], [43], and [44], the multtarget differentiation and vital sign detection are realized using the beamforming technology. However, they only focus

TABLE V
COMPARISON OF THIS ARTICLE WITH OTHER RELEVANT WORKS

Ref#	Radar Type	MIMO Configuration	Operating Frequency	Measure Parameters	Features
[30]	CW	4Tx4R & 8Tx8R	2.47 GHz	Human Position	Point target ¹
[27]	CW	4Tx4R	2.4 GHz	RR ²	Point target & Only RR monitoring
[29]	CW	1Tx8R	5.8 GHz	RR	Point target & Only RR monitoring
[43]	UWB	1Tx4R	60.5 GHz	RR	Point target & Only RR monitoring
[44]	Pulse	16Tx16R	36.44 GHz	RR	Point target & Only RR monitoring
[33]	FMCW	3Tx4R	77 GHz	RR & HR ³	Point target & Subjects breathe alternately
[45]	*	2Tx8R	120 GHz	RR & HR	Point target & Subjects at different distances
This work	IF-CW	6Tx6R	2.4 GHz	RR & HR	Accurate chest localization & Simultaneous monitoring of targets at the same distance

¹ Human is positioned as a point target

² Respiratory Rate

³ Heart Rate

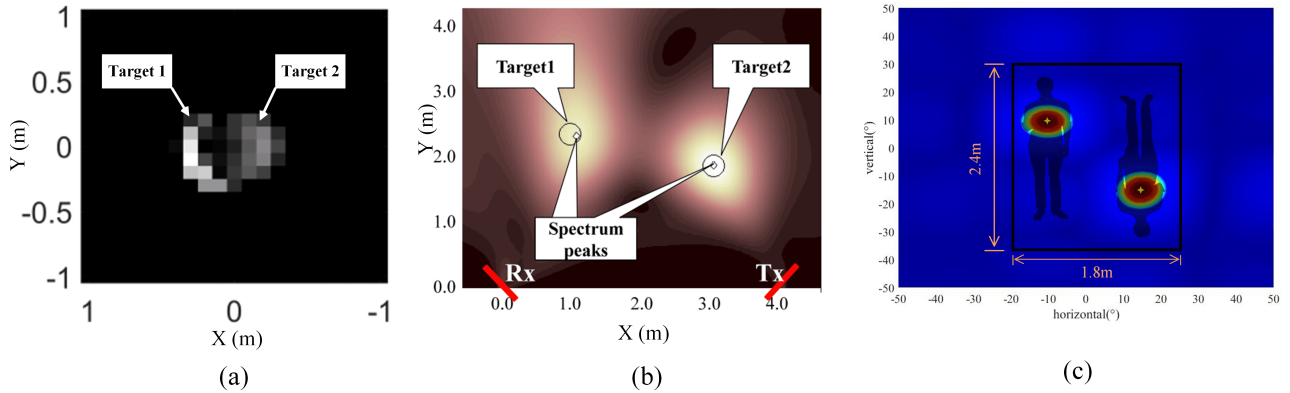


Fig. 18. Comparison of imaging results between this work and other relevant works. (a) Imaging result of two targets, modified based on [45]. (b) Imaging result of two targets, modified based on [30]. (c) Imaging result of this work.

on respiratory rate detection and do not involve heartbeat measurement. In [33] and [45], the respiratory and heart rates measurement of two targets is achieved with the portable MIMO radars. However, the limitation of [33] is that two subjects need to breathe alternately during the measurement. Similarly, in [43], two subjects need to take turns lying in bed for measurement and then linearly added the received signals to emulate the situation when there are two closely spaced patients. The limitation of [45] is that two subjects need to stand at different ranges from the radar system. Therefore, although the multitarget heartbeat measurement is achieved by these solutions, they are not suitable for applications in sleep monitoring scenarios in home care, e.g., sleep quality monitoring and sleep apnea detection, where two targets are close to each other. On the contrary, the vital signs of two closely spaced targets can be measured simultaneously by our radar system, as shown in Figs. 15(a) and 16. It provides a good solution for noncontact vital signs measurement of multiple targets in sleep monitoring scenarios.

Furthermore, in all these studies mentioned above, the human body is treated as a point target. Although they

can separate multiple subjects by imaging the scene, they are unable to locate specific parts of the humans, such as the chest cavity. For example, the imaging results mentioned in [45] and [30] are shown in Fig. 18(a) and (b), respectively. It results in tiny movements from all parts of the human body being received by the radar, e.g., random movements from legs, head, and arms, which will seriously affect vital signs measurement. In this article, the human body is treated as a body target. The chest areas of multiple targets are accurately located, as shown in Fig. 18(c). Then, the multitarget vital signs measurement, especially heartbeat measurement, is significantly enhanced by forming individual narrow beams focusing on the chest regions.

C. Future Work

As shown in the above results, the angular resolution of radar is an important metric in distinguishing different subjects. There are two main solutions to improve the resolution. One way is to design a nonuniformly spaced array. The antennas of the array are arranged sparsely with the designed

distance between two adjacent ones. The resolution improvement of this approach is limited. Another straightforward way is to increase the number of elements of the array. Since the width of the beam formed by radar is inversely proportional to the size of the antenna array, the increase in the number of T/R channels can directly improve the angular resolution of the radar.

However, additional antennas would increase the size of radar system and introduce more time consumption due to the TDM scheme adopted in the transmitter chain. In the future work, higher frequency (e.g., 24 GHz) would be adopted to reduce the system size. Moreover, orthogonal frequency-division multiplexing (OFDM) would be considered as an alternate of TDM [41]. With OFDM, signals with different carrier frequencies could be transmitted by different channels simultaneously. Then, in the receiving chain, a set of matched filter banks are used to separate the echo signals from different transmitters. In this way, a larger array providing higher angular resolution could be involved without increasing the scanning time of the system.

VI. CONCLUSION

In this article, an MIMO CW radar prototype is designed to achieve vital signs measurement of multiple targets. The radar system consists of six transmitting channels and six receiving channels. The 2-D DBF is realized by implementing the concept of MIMO to synthesize a planar array. Through 2-D beam scanning of the scene, an image is generated to separate multiple targets and locate the chest motion of targets accurately. Finally, the vital signs are obtained by forming individual beams to focus on these ROIs. Experimental results demonstrate that the proposed system can accurately locate the chest motion of two targets in different scenarios and the vital signs measured by the radar are in full agreement with the ground truth. Potential applications of the proposed MIMO radar system can be sleep monitoring, nurse room, and home healthcare monitoring.

REFERENCES

- [1] T. Martin, E. Jovanov, and D. Raskovic, "Issues in wearable computing for medical monitoring applications: A case study of a wearable ECG monitoring device," in *Proc. Dig. Papers. 4th Int. Symp. Wearable Comput.*, 2000, pp. 43–49.
- [2] H. Hong *et al.*, "Microwave sensing and sleep: Noncontact sleep-monitoring technology with microwave biomedical radar," *IEEE Microw. Mag.*, vol. 20, no. 8, pp. 18–29, Aug. 2019.
- [3] M. Nosrati and N. Tavassolian, "High-accuracy heart rate variability monitoring using Doppler radar based on Gaussian pulse train modeling and FTPR algorithm," *IEEE Trans. Microw. Theory Techn.*, vol. 66, no. 1, pp. 556–567, Jan. 2018.
- [4] C. Gu, Z. Peng, and C. Li, "High-precision motion detection using low-complexity Doppler radar with digital post-distortion technique," *IEEE Trans. Microw. Theory Techn.*, vol. 64, no. 3, pp. 961–971, Mar. 2016.
- [5] M. Mercuri, Y.-H. Liu, I. Lorato, T. Torfs, A. Bourdoux, and C. Van Hoof, "Frequency-tracking CW Doppler radar solving small-angle approximation and null point issues in non-contact vital signs monitoring," *IEEE Trans. Biomed. Circuits Syst.*, vol. 11, no. 3, pp. 671–680, Jun. 2017.
- [6] Y. Wang, Q. Liu, and A. E. Fathy, "CW and pulse-Doppler radar-processing based on FPGA for human sensing applications," *IEEE Trans. Geosci. Remote Sens.*, vol. 51, no. 5, pp. 3097–3107, May 2013.
- [7] G. Wang, J.-M. Munoz-Ferreras, C. Gu, C. Li, and R. Gomez-Garcia, "Application of linear-frequency-modulated continuous-wave (LFMCW) radars for tracking of vital signs," *IEEE Trans. Microw. Theory Techn.*, vol. 62, no. 6, pp. 1387–1399, Jun. 2014.
- [8] M. Nosrati and N. Tavassolian, "Accuracy enhancement of Doppler radar-based heartbeat rate detection using chest-wall acceleration," in *Proc. IEEE Int. Microw. Biomed. Conf. (IMBioC)*, Philadelphia, PA, USA, Jun. 2018, pp. 139–141.
- [9] T. Sakamoto *et al.*, "Feature-based correlation and topological similarity for interbeat interval estimation using ultrawideband radar," *IEEE Trans. Biomed. Eng.*, vol. 63, no. 4, pp. 747–757, Apr. 2016.
- [10] L. Sun *et al.*, "Noncontact vital sign detection based on stepwise atomic norm minimization," *IEEE Signal Process. Lett.*, vol. 22, no. 12, pp. 2479–2483, Dec. 2015.
- [11] M. Mercuri, I. R. Lorato, Y.-H. Liu, F. Wieringa, C. V. Hoof, and T. Torfs, "Vital-sign monitoring and spatial tracking of multiple people using a contactless radar-based sensor," *Nature Electron.*, vol. 2, no. 6, pp. 252–262, Jun. 2019.
- [12] G.-W. Fang, C.-Y. Huang, and C.-L. Yang, "Switch-based low intermediate frequency system of a vital sign radar for simultaneous multitarget and multidirectional detection," *IEEE J. Electromagn., RF Microw. Med. Biol.*, vol. 4, no. 4, pp. 265–272, Dec. 2020.
- [13] M. Mercuri, Y.-H. Liu, S. Sheelavant, S. Polito, T. Torfs, and C. Van Hoof, "Digital linear discrete FMCW radar for healthcare applications," in *IEEE MTT-S Int. Microw. Symp. Dig.*, Jun. 2019, pp. 144–147.
- [14] F.-K. Wang, P.-H. Juan, D.-M. Chian, and C.-K. Wen, "Multiple range and vital sign detection based on single-conversion self-injection-locked hybrid mode radar with a novel frequency estimation algorithm," *IEEE Trans. Microw. Theory Techn.*, vol. 68, no. 5, pp. 1908–1920, May 2020.
- [15] H. Lee, B.-H. Kim, J.-K. Park, S. W. Kim, and J.-G. Yook, "A resolution enhancement technique for remote monitoring of the vital signs of multiple subjects using a 24 GHz bandwidth-limited FMCW radar," *IEEE Access*, vol. 8, pp. 1240–1248, 2020.
- [16] H. Lee, B.-H. Kim, J.-K. Park, and J.-G. Yook, "A novel vital-sign sensing algorithm for multiple subjects based on 24-GHz FMCW Doppler radar," *Remote Sens.*, vol. 11, no. 10, p. 1237, May 2019.
- [17] G.-W. Fang, C.-Y. Huang, and C.-L. Yang, "Simultaneous detection of multi-target vital signs using EEMD algorithm based on FMCW radar," in *IEEE MTT-S Int. Microw. Symp. Dig.*, May 2019, pp. 1–4.
- [18] W.-C. Su, M.-C. Tang, R. E. Arif, T.-S. Horng, and F.-K. Wang, "Stepped-frequency continuous-wave radar with self-injection-locking technology for monitoring multiple human vital signs," *IEEE Trans. Microw. Theory Techn.*, vol. 67, no. 12, pp. 5396–5405, Dec. 2019.
- [19] S. Nahar, T. Phan, F. Quaiyum, L. Ren, A. E. Fathy, and O. Kilic, "An electromagnetic model of human vital signs detection and its experimental validation," *IEEE J. Emerg. Sel. Topics Circuits Syst.*, vol. 8, no. 2, pp. 338–349, Jun. 2018.
- [20] Q. Deng, J. Le, S. Barbat, R. Tian, and Y. Chen, "Efficient living subject localization and weak vital-sign signal enhancement using impulse radio based UWB radar," in *Proc. IEEE Intell. Vehicles Symp. (IV)*, Jun. 2019, pp. 777–782.
- [21] Y. Yang, J. Cao, X. Liu, and X. Liu, "Multi-breath: Separate respiration monitoring for multiple persons with UWB radar," in *Proc. IEEE 43rd Annu. Comput. Softw. Appl. Conf. (COMPSAC)*, Jul. 2019, pp. 840–849.
- [22] S. Wu *et al.*, "Study on a novel UWB linear array human respiration model and detection method," *IEEE J. Sel. Topics Appl. Earth Observ. Remote Sens.*, vol. 9, no. 1, pp. 125–140, Jan. 2016.
- [23] C. Lu, Y. Yuan, C.-H. Tseng, and C.-T. Michael Wu, "Multi-target continuous-wave vital sign radar using 24 GHz metamaterial leaky wave antennas," in *IEEE MTT-S Int. Microw. Symp. Dig.*, May 2019, pp. 1–4.
- [24] Y. Yuan, C. Lu, A. Y.-K. Chen, C.-H. Tseng, and C.-T.-M. Wu, "Noncontact multi-target vital sign detection using self-injection-locked radar sensor based on metamaterial leaky wave antenna," in *IEEE MTT-S Int. Microw. Symp. Dig.*, Jun. 2019, pp. 148–151.
- [25] Q. Li, Y. Zhang, and C. M. Wu, "Noncontact vital sign detection using 24 GHz two-dimensional frequency scanning metamaterial leaky wave antenna array," in *IEEE MTT-S Int. Microw. Symp. Dig.*, Jun. 2018, pp. 255–258.
- [26] Y. Yuan, C. Lu, A. Y.-K. Chen, C.-H. Tseng, and C.-T.-M. Wu, "Multi-target concurrent vital sign and location detection using metamaterial-integrated self-injection-locked quadrature radar sensor," *IEEE Trans. Microw. Theory Techn.*, vol. 67, no. 12, pp. 5429–5437, Dec. 2019.

- [27] M. Nosrati, S. Shahsavari, S. Lee, H. Wang, and N. Tavassolian, “A concurrent dual-beam phased-array Doppler radar using MIMO beamforming techniques for short-range vital-signs monitoring,” *IEEE Trans. Antennas Propag.*, vol. 67, no. 4, pp. 2390–2404, Apr. 2019.
- [28] C. Hsu, C. Chuang, F. Wang, T. Horng, and L. Hwang, “Detection of vital signs for multiple subjects by using self-injection-locked radar and mutually injection-locked beam scanning array,” in *IEEE MTT-S Int. Microw. Symp. Dig.*, Jun. 2017, pp. 991–994.
- [29] J. Xiong, H. Zhang, H. Hong, H. Zhao, X. Zhu, and C. Li, “Multi-target vital signs detection using SIMO continuous-wave radar with DBF technique,” in *Proc. IEEE Radio Wireless Symp. (RWS)*, Jan. 2020, pp. 194–196.
- [30] D. Sasakawa, N. Honma, T. Nakayama, and S. Iizuka, “Fast living-body localization algorithm for MIMO radar in multipath environment,” *IEEE Trans. Antennas Propag.*, vol. 66, no. 12, pp. 7273–7281, Dec. 2018.
- [31] S. Hasebe, D. Sasakawa, K. Kishimoto, and N. Honma, “Simultaneous detection of multiple targets’ vital signs using MIMO radar,” in *Proc. Int. Symp. Antennas Propag. (ISAP)*, Oct. 2018, pp. 1–2.
- [32] D. Sasakawa, N. Honma, T. Nakayama, and S. Iizuka, “Human posture identification using a MIMO array,” *Electronics*, vol. 7, no. 3, p. 37, Mar. 2018.
- [33] A. Ahmad, J. C. Roh, D. Wang, and A. Dubey, “Vital signs monitoring of multiple people using a FMCW millimeter-wave sensor,” in *Proc. IEEE Radar Conf. (RadarConf)*, Oklahoma City, OK, USA, Apr. 2018, pp. 1450–1455.
- [34] T. Sakamoto and T. Koda, “Respiratory motion imaging using 2.4-GHz nine-element-array continuous-wave radar,” *IEEE Microw. Wireless Compon. Lett.*, vol. 30, no. 7, pp. 717–720, Jul. 2020.
- [35] Y. Liu, S. Wu, J. Chen, G. Fang, and H. Yin, “Human respiration localization method using UWB linear antenna array,” *J. Sensors*, vol. 2015, Feb. 2015, Art. no. 601926, doi: [10.1155/2015/601926](https://doi.org/10.1155/2015/601926).
- [36] S. M. M. Islam, O. Boric-Lubecke, and V. M. Lubekce, “Concurrent respiration monitoring of multiple subjects by phase-comparison monopulse radar using independent component analysis (ICA) with JADE algorithm and direction of arrival (DOA),” *IEEE Access*, vol. 8, pp. 73558–73569, Apr. 2020, doi: [10.1109/ACCESS.2020.2988038](https://doi.org/10.1109/ACCESS.2020.2988038).
- [37] F. C. Robey, S. Coutts, D. Weikle, J. C. McHarg, and K. Cuomo, “MIMO radar theory and experimental results,” in *Proc. Conf. Rec. 38th Asilomar Conf. Signals, Syst. Comput.*, vol. 1, 2004, pp. 300–304.
- [38] I. Mostafanezhad and O. Boric-Lubecke, “Benefits of coherent low-IF for vital signs monitoring using Doppler radar,” *IEEE Trans. Microw. Theory Techn.*, vol. 62, no. 10, pp. 2481–2487, Oct. 2014.
- [39] H. Zhao, H. Hong, L. Sun, Y. Li, C. Li, and X. Zhu, “Noncontact physiological dynamics detection using low-power digital-IF Doppler radar,” *IEEE Trans. Instrum. Meas.*, vol. 66, no. 7, pp. 1780–1788, Jul. 2017.
- [40] Z. Peng and C. Li, “A portable K-band 3-D MIMO radar with nonuniformly spaced array for short-range localization,” *IEEE Trans. Microw. Theory Techn.*, vol. 66, no. 11, pp. 5075–5086, Nov. 2018.
- [41] H. Forsten, T. Kiuru, M. Hirvonen, M. Varonen, and M. Kaynak, “Scalable 60 GHz FMCW frequency-division multiplexing MIMO radar,” *IEEE Trans. Microw. Theory Techn.*, vol. 68, no. 7, pp. 2845–2855, Jul. 2020.
- [42] M. L. Skolnik, *Radar Handbook*, 3rd ed. New York, NY, USA: McGrawHill, 2008.
- [43] M. Muragaki *et al.*, “Noncontact respiration monitoring of multiple closely positioned patients using ultra-wideband array radar with adaptive beamforming technique,” in *Proc. IEEE Int. Conf. Acoust., Speech Signal Process. (ICASSP)*, New Orleans, LA, USA, Mar. 2017, pp. 1118–1122.
- [44] O. Bialawons and J. Klare, “Person localization by detection of breathing with the MIMO radar MIRA-CLE Ka,” in *Proc. 10th Eur. Conf. Synth. Aperture Radar (EUSAR)*, Berlin, Germany, Jun. 2014, pp. 1–4.
- [45] S. Wang, S. Kueppers, H. Cetinkaya, and R. Herschel, “3D localization and vital sign detection of human subjects with a 120 GHz MIMO radar,” in *Proc. 20th Int. Radar Symp. (IRS)*, Ulm, Germany, Jun. 2019, pp. 1–6.
- [46] E. Cardillo and A. Caddemi, “A review on biomedical MIMO radars for vital sign detection and human localization,” *Electronics*, vol. 9, no. 9, p. 1497, Sep. 2020.